

THE RADIAL ACCELERATION RELATION IN CLASH GALAXY CLUSTERS

YONG TIAN¹, KEIICHI UMETSU², CHUNG-MING KO^{1,3}, MEGAN DONAHUE⁴, AND I-NON CHIU²

Draft version February 2, 2022

ABSTRACT

The radial acceleration relation (RAR) in galaxies describes a tight empirical scaling law between the total acceleration $g_{\text{tot}}(r) = GM_{\text{tot}}(< r)/r^2$ observed in galaxies and that expected from their baryonic mass $g_{\text{bar}}(r) = GM_{\text{bar}}(< r)/r^2$, with a characteristic acceleration scale of $g_{\dagger} \simeq 1.2 \times 10^{-10} \text{ m s}^{-2}$. Here, we examine if such a correlation exists in galaxy clusters using weak-lensing, strong-lensing, and X-ray data sets available for 20 high-mass clusters targeted by the CLASH survey. By combining our CLASH data with stellar mass estimates for the brightest cluster galaxies (BCGs) and accounting for the stellar baryonic component in clusters, we determine, for the first time, an RAR on BCG–cluster scales. The resulting RAR is well described by a tight power-law relation, $g_{\text{tot}} \propto g_{\text{bar}}^{0.51^{+0.04}_{-0.05}}$, with lognormal intrinsic scatter of $14.7^{+2.9}_{-2.8}\%$. The slope is consistent with the low acceleration limit of the RAR in galaxies, $g_{\text{tot}} = \sqrt{g_{\dagger} g_{\text{bar}}}$, whereas the intercept implies a much higher acceleration scale of $g_{\ddagger} = (2.02 \pm 0.11) \times 10^{-9} \text{ m s}^{-2}$, indicating that there is no universal RAR that holds on all scales from galaxies to clusters. We find that the observed RAR in CLASH clusters is consistent with predictions from a semi-analytical model developed in the standard Λ CDM framework. Our results also predict the presence of a baryonic Faber–Jackson relation ($\sigma_v^4 \propto M_{\text{bar}}$) on cluster scales.

1. INTRODUCTION

Clusters of galaxies exhibit a large mass discrepancy between baryonic and gravitational mass. Understanding the nature and amount of unseen mass in galaxy clusters is a long-standing issue in astrophysics. Zwicky (1933) was the first to analyze dynamics of the Coma cluster and to infer the existence of “dark matter” (DM). The vast majority of baryons (80–90%) in galaxy clusters are in the form of X-ray emitting diffuse hot gas. The gas mass fraction in high-mass galaxy clusters is observed to reach $\simeq 13\%$ in the intracluster region (e.g., Vikhlinin et al. 2006; Umetsu et al. 2009; Planck Collaboration et al. 2013; Donahue et al. 2014), and their global mass content is dominated by DM ($\sim 85\%$). Moreover, cold dark matter (CDM) that dominates the matter budget of the universe is essential to explain a range of cosmological probes on larger scales, such as cosmic microwave background anisotropy, large-scale galaxy clustering, and weak-lensing cosmic-shear observations. The current concordance cosmological paradigm, Λ CDM, also assumes a cosmological constant (Λ) to account for the late-time accelerated expansion of the universe in the framework of general relativity.

At the scales of spiral galaxies, the discrepancy between baryonic and dynamical mass, $M_{\text{tot}}(< r)/M_{\text{bar}}(< r)$, is found to tightly couple with gravitational acceleration, but no obvious correlation with other physical quantities, such as the size and orbital frequency, was found so far (e.g., McGaugh 2004). The mass ratio $M_{\text{tot}}(< r)/M_{\text{bar}}(< r)$ increases sys-

tematically with decreasing acceleration below a characteristic scale of $\simeq 10^{-10} \text{ m s}^{-2}$. This is referred to as the mass discrepancy–acceleration relation (MDAR; for a review, see, e.g., Famaey & McGaugh 2012).

In the case of spiral galaxies, the low acceleration limit gives a baryonic Tully–Fisher relation and an acceleration scale that is consistent with the MDAR (McGaugh 2011). Using a sample of 153 disk galaxies from the SPARC database (Lelli et al. 2016), McGaugh et al. (2016) found a tight radial acceleration relation (RAR) between the observed total acceleration $g_{\text{tot}} = GM_{\text{tot}}(< r)/r^2$ and the baryonic acceleration $g_{\text{bar}} = GM_{\text{bar}}(< r)/r^2$ defined at the same galacto-centric radius r as

$$\frac{g_{\text{tot}}}{g_{\text{bar}}} = \frac{M_{\text{tot}}}{M_{\text{bar}}} = \frac{1}{1 - e^{-\sqrt{g_{\text{bar}}/g_{\dagger}}}}, \quad (1)$$

where $g_{\dagger} = 1.20 \pm 0.02$ (stat.) ± 0.24 (syst.) $\times 10^{-10} \text{ m s}^{-2}$. The low acceleration limit ($g_{\text{bar}} \ll g_{\dagger}$) of Equation (1) gives the following power-law relation:

$$g_{\text{tot}} = \sqrt{g_{\dagger} g_{\text{bar}}}. \quad (2)$$

Similarly, the MDAR (Scarpa 2006; Janz et al. 2016; Tian & Ko 2016) and the RAR observed in elliptical galaxies are consistent with those of spiral galaxies (Lelli et al. 2017; Rong et al. 2018; Chae et al. 2019; Milgrom 2019; Tian & Ko 2019). Moreover, the MDAR of 53 elliptical galaxies obtained from strong-lens modeling of Einstein rings is consistent with the dynamical results (Tian & Ko 2017).

The RAR observed on galaxy scales raises four issues to be addressed (Desmond 2017; Lelli et al. 2017): (1) the characteristic acceleration scale g_{\dagger} ; (2) the slope in the small acceleration limit ($\simeq 0.5$); (3) the tightness of intrinsic scatter of the relation (0.11 dex); (4) no correlation with other galactic properties. Possible explanations of the above issues can be classified into the following three categories (McGaugh et al. 2016; Lelli et al. 2017): (I) galaxy formation processes in the Λ CDM model; (II) new “dark sector” physics; and (III) new

yongtian@gm.astro.ncu.edu.tw

keiichi@asiaa.sinica.edu.tw

cmko@gm.astro.ncu.edu.tw

¹ Institute of Astronomy, National Central University, Taoyuan 32001, Taiwan² Academia Sinica Institute of Astronomy and Astrophysics (ASIAA), No. 1, Section 4, Roosevelt Road, Taipei 10617, Taiwan³ Department of Physics and Center for Complex Systems, National Central University, Taoyuan 32001, Taiwan⁴ Physics and Astronomy Department, Michigan State University, East Lansing, MI 48824, USA

dynamical laws.

In the Λ CDM framework, baryonic mass dominated by stars is bound to the gravitational potential well of the DM halo hosting a galaxy. However, the baryons are re-distributed through complex galaxy formation processes, such as active galactic nuclei (AGN) feedback, stellar winds, and supernova explosions. Several attempts have been made to explain the observed RAR in the context of Λ CDM through hydrodynamical simulations (Wu & Kroupa 2015; Ludlow et al. 2017) and semi-empirical models of galaxy formation (Di Cintio & Lelli 2016; Navarro et al. 2017; Desmond 2017) by adopting an abundance matching relation (Behroozi et al. 2013). Besides the standard CDM paradigm, some considered baryon-DM coupling in a dark-fluid framework (Zhao & Li 2010; Khoury 2015) or dipolar DM particles (Blanchet & Le Tiec 2008, 2009).

Alternatively, the RAR has been interpreted as a consequence of a new dynamical law without the need of DM. Milgrom (1983) introduced modified Newtonian dynamics (MOND), in which the dynamical law changes with an acceleration scale g_\dagger . However, MOND cannot explain the dynamics of galaxy clusters, and it needs to account for a large missing mass of about a factor of two (Pointecouteau & Silk 2005; Sanders 1999, 2003).

The four issues posed by the RAR observed in galaxies also represent some challenges to the Λ CDM model (Desmond 2017; Lelli et al. 2017). Wu & Kroupa (2015) found that simulation results do not match well the data presented in McGaugh (2004). Ludlow et al. (2017) successfully reproduced (2) and (4) within the Λ CDM framework, but with an acceleration scale $2.2g_\dagger$, which is significantly higher than the observed value (Li et al. 2018). Di Cintio & Lelli (2016) explained (1) and (2) by introducing an abundance matching prescription, whereas the level of scatter is significantly larger than the observed value, and the residuals are correlated with the galacto-centric radius. Desmond (2017) used more sophisticated model but got still larger scatter even using zero scatter in abundance matching.

How about galaxy clusters? Navarro et al. (2017) argued in the Λ CDM framework that the RAR in galaxy clusters (if exists) should be deviated from that of galaxies because the central maximum halo acceleration exceeds g_\dagger ($\simeq 3 \times 10^{-10} \text{ m s}^{-2}$). On the other hand, MOND predicts the RAR in galactic systems. Its failure in galaxy clusters would pose a significant challenge to MOND (Famaey & McGaugh 2012). Although the RAR is well studied in galactic systems, it has never been explored in galaxy clusters.

In this paper, we present an RAR in 20 high-mass galaxy clusters based on high-quality multiwavelength data sets available for the CLASH survey. The paper is organized as follows. In Section 2, we summarize the characteristics of the CLASH sample and the data products. In Section 3, we present the radial profiles of the baryon fraction and the RAR for the CLASH sample. In Section 4, we discuss the results and implications of our findings. Finally a summary is given in Section 5.

Throughout this paper, we assume a flat Λ CDM cosmology with $\Omega_m = 0.27$, $\Omega_\Lambda = 0.73$, and a Hubble constant of $H_0 = 100h \text{ km s}^{-1} \text{ Mpc}^{-1}$ with $h = 0.7$. We denote the critical density of the universe at a particular redshift z as $\rho_c(z) = 3H^2(z)/(8\pi G)$, with $H(z)$ the redshift-dependent Hubble parameter. We adopt the standard notation M_Δ to denote the mass enclosed within a sphere of radius

r_Δ within which the mean overdensity equals $\Delta \times \rho_c(z)$. That is, $M_\Delta = (4\pi\Delta/3)\rho_c(z)r_\Delta^3$. We define the gravitational acceleration in the framework of Newtonian dynamics as $g(r) = GM(< r)/r^2$.

2. CLUSTER SAMPLE AND DATA

We analyze multiwavelength data products from the Cluster Lensing And Supernova survey with Hubble (CLASH; Postman et al. 2012). The CLASH survey is a 524-orbit *Hubble Space Telescope* (HST) Multi-Cycle Treasury program designed to probe the mass distribution of 25 high-mass galaxy clusters with $M_{500} \gtrsim 4 \times 10^{14} M_\odot$ (Umetsu et al. 2016). In this sample, 20 clusters were X-ray selected to be hot ($T_X > 5 \text{ keV}$) and to have a regular X-ray morphology. Numerical simulations suggest that the X-ray-selected subsample is largely composed of relaxed clusters ($\sim 70\%$), but it also contains a nonnegligible fraction ($\sim 30\%$) of unrelaxed systems (Meneghetti et al. 2014). Another subset of five clusters were selected by their lensing properties to produce high-magnification events. These clusters often turn out to be dynamically disturbed merging systems.

In this study, we focus on a subset of 20 CLASH clusters taken from Umetsu et al. (2016), who presented a joint analysis of strong-lensing, weak-lensing shear and magnification data of these individual clusters. Among the 20 clusters, 16 are X-ray selected, and the rest are high-magnification systems. The full-lensing analysis of Umetsu et al. (2016) combined constraints from 16-band HST observations (Zitrin et al. 2015) and wide-field multicolor imaging taken primarily with Suprime-Cam on the Subaru telescope (Umetsu et al. 2014). For all clusters in the CLASH sample, Donahue et al. (2014) derived binned radial profiles of temperature, gas mass, and hydrostatic mass using *Chandra* and *XMM-Newton* X-ray observations.

Here we combine the total mass measurements M_{tot} of Umetsu et al. (2016) based on strong and weak lensing (Section 2.1) and the X-ray gas mass measurements M_{gas} of Donahue et al. (2014) to study the relationship between the total and baryonic acceleration profiles. Moreover, we statistically account for the stellar contribution to the baryonic acceleration (Section 2.2). We also include stellar mass estimates for the central brightest cluster galaxies (BCGs; Section 2.3).

2.1. Lensing Mass

Combining the strong lensing, weak lensing shear and magnification effects, Umetsu et al. (2016) reconstructed the surface mass density profile of each individual cluster over a wide range of the cluster-centric radius. Umetsu et al. (2016) found that the ensemble-averaged total mass distribution of the CLASH sample is well described by a family of cuspy, outward-steepening density profiles, namely, the Navarro–Frenk–White (NFW, hereafter; Navarro et al. 1997), Einasto, and DARKexp (Hjorth & Williams 2010) models. Of these, the NFW model best describes the CLASH lensing data (e.g., Umetsu et al. 2011b; Umetsu & Diemer 2017). On the other hand, the single power-law, cored isothermal, and Burkert profiles were statistically disfavored by the observed CLASH lensing profile having a pronounced radial curvature (Umetsu et al. 2016).

Here we use the CLASH lensing constraints on the total mass profile $M_{\text{tot}}(< r)$ of each individual CLASH cluster assuming a spherical NFW profile. The total mass $M_{\text{tot}}(< r)$ of an NFW halo as a function of spherical radius r is written

as

$$M_{\text{tot}}(< r | M_{200}, c_{200}) = 4\pi\rho_s r_s^3 \left[\ln\left(1 + \frac{r}{r_s}\right) - \frac{r}{r + r_s} \right], \quad (3)$$

where r_s and ρ_s represent the characteristic scale radius and density of the NFW profile, respectively, and ρ_s is given by

$$\rho_s = \frac{200}{3} \frac{c_{200}^3}{\ln(1 + c_{200}) - c_{200}/(1 + c_{200})} \rho_c(z) \quad (4)$$

with $c_{200} \equiv r_{200}/r_s$ the NFW concentration parameter.

For each cluster, Umetsu et al. (2016) extracted the posterior probability distributions of (M_{200}, c_{200}) from the observed surface mass density profile assuming a spherical NFW halo, by accounting for all relevant sources of uncertainty (e.g., Umetsu et al. 2016, 2020; Miyatake et al. 2019): (i) measurement errors, (ii) cosmic noise due to projected large-scale structure uncorrelated with the cluster, (iii) statistical fluctuations of the projected cluster lensing signal due to halo triaxiality and correlated substructures. According to cosmological hydrodynamical simulations of Meneghetti et al. (2014), the CLASH sample selection is expected to be largely free from orientation bias. In fact, three-dimensional full-triaxial analyses of CLASH lensing observations found no statistical evidence for orientation bias in the CLASH sample (see Sereno et al. 2018; Chiu et al. 2018). Therefore, assuming spherical NFW halos is not expected to cause any significant bias in lensing mass estimates of the CLASH sample. The mass and concentration parameters (M_{200}, c_{200}) of each individual CLASH cluster are summarized in Table 2 of Umetsu et al. (2016).

In our analysis, we use these posterior distributions of the NFW parameters to obtain well-characterized inference of $M_{\text{tot}}(< r | M_{200}, c_{200})$ for each individual cluster. We compute the total mass profile $M_{\text{tot}}(< r | M_{200}, c_{200})$ and its uncertainty of each cluster in the radial range at $r \geq r_{\text{min}} \simeq 14 \text{ kpc}$.

2.2. Baryonic Mass

The X-ray emitting hot gas dominates the baryonic mass in galaxy clusters. In high-mass clusters, more than 80% of the intra-cluster baryons are in the X-ray emitting hot phase (e.g., Umetsu et al. 2009; Donahue et al. 2014; Okabe et al. 2014; Chiu et al. 2018). Donahue et al. (2014) derived enclosed gas mass profiles $M_{\text{gas}}(< r)$ for all CLASH clusters, finding that the M_{gas} profiles measured from the *Chandra* and *XMM* observations are in excellent agreement where the data overlap. Since *XMM* data are not available for all the clusters, we only use *Chandra* M_{gas} measurements of Donahue et al. (2014) as primary constraints on the baryonic mass content in the CLASH sample. For each cluster, we have measured $M_{\text{gas}}(< r)$ values in several radial bins, where the radial range is different for each cluster, depending on the redshift and the data quality (see Figure 1).

We then account for the stellar contribution to the baryonic mass using the results of Chiu et al. (2018), who established the stellar-to-gas mass relation $f_c(r) = M_{\text{star}}/(M_{\text{gas}} + M_{\text{star}})$ (see their Figure 11; f_c referred to as the cold collapsed baryonic fraction), for a sample of 91 Sunyaev-Zel'dovich effect (SZE) clusters with $M_{500} > 2.5 \times 10^{14} M_{\odot}$ selected from the South Pole Telescope (SPT) survey (Carlstrom et al. 2011; Bleem et al. 2015). The $f_c(r)$ relation is insensitive to the cluster redshift over a broad range out to

$z \sim 1.3$ as probed by the SPT sample. In their study, the total masses were estimated from the SZE observable, the gas masses M_{gas} from *Chandra* X-ray data, and the stellar masses M_{star} from combined optical/near-infrared multi-band photometry. The $f_c(r)$ relation of Chiu et al. (2018) includes the stellar mass contributions from the BCG and cluster member galaxies inside the r_{500} overdensity radius.

With the mean $f_c(r)$ relation, we estimate the total baryonic mass as $M_{\text{bar}}(< r) = M_{\text{gas}}(< r)/[1 - f_c(r)]$, ignoring the cluster-to-cluster scatter. The level of scatter around the mean $f_c(r)$ relation is about 12%.

2.3. BCG Stellar Mass

In the central cluster region, the baryonic mass in clusters is dominated by the stellar mass in the BCG. In this study, we model the stellar mass distribution of each BCG with the Hernquist model (Hernquist 1990), which gives an analytical approximation to the deprojected form of de Vaucouleurs' profile (or a Sérsic profile with index $n = 4$). Then, the stellar mass $m_{\text{star}}(< r)$ inside the spherical radius r and the stellar gravitational acceleration $g_{\text{star}}(< r)$ are expressed as

$$m_{\text{star}}(< r) = \frac{\mathcal{M}_{\text{star}} r^2}{(r + r_h)^2}, \quad (5)$$

$$g_{\text{star}}(r) = \frac{G \mathcal{M}_{\text{star}}}{(r + r_h)^2},$$

where $\mathcal{M}_{\text{star}}$ is the total stellar mass of the BCG, and $r_h \approx 0.551 R_e$ is a characteristic scale length of the Hernquist model, with R_e the half-light or effective radius of the de Vaucouleurs' brightness profile.

In this study, we adopt as $\mathcal{M}_{\text{star}}$ (see Table 1) the stellar mass estimates of CLASH BCGs from Cooke et al. (2016, their Table 1), who performed a multiwavelength analysis on a large sample of BCGs by combining UV, optical, near-infrared, and far-infrared data sets. Since the measurement errors on BCG stellar masses were not provided in Cooke et al. (2016), we assume a fractional uncertainty of 10% on $\mathcal{M}_{\text{star}}$.

We measure the BCG effective radius R_e from the CLASH *HST* imaging using the GALFIT package (Peng et al. 2010). We choose to measure R_e of each BCG in the *HST* band corresponding to the rest-frame wavelength of $1 \mu\text{m}$. The corresponding *HST* bands for our sample ($0.187 \leq z \leq 0.686$) are all in the WFC3/IR coverage (F110W to F160W), as summarized in Table 1. We fit a single Sérsic profile to the surface brightness distribution of the BCG in the CLASH *HST* imaging data. The initial guess of the BCG position is based on the rest-frame UV (280 nm) measurements of Donahue et al. (2015). In Table 1, we also list the final source position (R.A., Decl.) in J2000 coordinates, Sérsic index (n), and effective radius (R_e) from our GALFIT modeling.

3. RESULTS

The key issue of the present study is to examine if the correlation between g_{tot} and g_{bar} is related to any physical or environmental parameters governing the system. A possible approach is to study the baryon-to-total acceleration ratio $g_{\text{bar}}(r)/g_{\text{tot}}(r)$, or the baryon fraction $f_{\text{bar}}(r)$, as a function of the cluster-centric radius r . An alternative approach is to examine the correlation between $g_{\text{tot}}(r)$ and $g_{\text{bar}}(r)$, namely the RAR.

3.1. Hot Gas Fraction

Table 1
Properties of BCGs in the CLASH sample

Cluster name	Redshift ^a	R.A. ^a (J2000.0)	Decl. ^a (J2000.0)	Band ^b	n^c	R_e^d (kpc)	r^e (kpc)	M_{star}^f ($10^{11} M_\odot$)	M_{gas}^g ($10^{11} M_\odot$)	M_{tot}^h ($10^{11} M_\odot$)
Abell 383	0.187	02 : 48 : 03.38	-03 : 31 : 45.02	F110W	2.34	17.0 ± 0.09	14.3	4.45	1.78 ± 0.09	7.55 ± 2.23
Abell 209	0.206	01 : 31 : 52.55	-13 : 36 : 40.50	F125W	2.62	22.1 ± 0.14	14.3	4.85	-	3.87 ± 0.79
Abell 2261	0.224	17 : 22 : 27.21	+32 : 07 : 57.62	F125W	1.74	18.7 ± 0.08	23.6	12.30	0.48 ± 0.03	6.44 ± 1.48
RX J2129.7+0005	0.234	21 : 29 : 39.96	+00 : 05 : 21.17	F125W	2.70	41.4 ± 0.54	14.3	5.81	2.18 ± 0.07	6.65 ± 1.91
Abell 611	0.288	08 : 00 : 56.82	+36 : 03 : 23.63	F125W	2.55	30.4 ± 0.16	22.2	6.58	0.48 ± 0.03	6.24 ± 1.81
MS2137-2353	0.313	21 : 40 : 15.16	-23 : 39 : 40.10	F125W	2.35	15.0 ± 0.04	14.3	3.65	2.94 ± 0.07	3.98 ± 1.57
RX J2248.7-4431	0.348	22 : 48 : 43.97	-44 : 31 : 51.14	F140W	2.45	34.5 ± 0.20	30.3	8.09	1.01 ± 0.03	6.19 ± 2.16
MACS J1115.9+0129	0.355	11 : 15 : 51.91	+01 : 29 : 55.00	F140W	3.83	52.9 ± 0.93	16.2	3.00	5.80 ± 0.19	6.25 ± 1.53
MACS J1931.8-2635	0.352	19 : 31 : 49.70	-26 : 34 : 32.22	F140W	3.49	33.2 ± 0.38	14.3	6.92	1.47 ± 0.02	7.21 ± 2.90
RX J1532.9+3021	0.362	15 : 32 : 53.78	+30 : 20 : 59.43	F140W	2.81	21.8 ± 0.14	14.3	3.34	1.13 ± 0.04	6.80 ± 4.18
MACS J1720.3+3536	0.387	17 : 20 : 16.75	+35 : 36 : 26.24	F140W	2.63	17.2 ± 0.06	23.6	6.59	1.15 ± 0.03	6.83 ± 2.07
MACS J0416.1-2403	0.397	04 : 16 : 09.15	-24 : 04 : 02.99	F140W	3.78	56.2 ± 0.81	14.3	3.14	-	4.22 ± 0.94
MACS J0429.6-0253	0.399	04 : 29 : 36.00	-02 : 53 : 06.78	F140W	1.80	29.3 ± 0.08	17.2	11.90	6.71 ± 0.55	9.98 ± 3.40
MACS J1206.2-0847	0.439	12 : 06 : 12.15	-08 : 48 : 03.32	F140W	3.65	44.8 ± 0.52	14.3	3.13	-	6.90 ± 2.07
MACS J0329.7-0211	0.450	03 : 29 : 41.57	-02 : 11 : 46.33	F140W	2.76	22.9 ± 0.12	22.2	8.47	13.1 ± 0.41	25.30 ± 6.50
RX J1347.5-1145	0.451	13 : 47 : 30.61	-11 : 45 : 09.33	F140W	2.62	21.7 ± 0.12	14.3	4.52	5.11 ± 0.07	7.28 ± 1.88
MACS J1149.5+2223	0.544	11 : 49 : 35.70	+22 : 23 : 54.68	F160W	2.44	34.3 ± 0.32	14.3	4.72	-	4.54 ± 1.12
MACS J0717.5+3745	0.548	07 : 17 : 32.52	+37 : 44 : 34.84	F160W	2.49	13.2 ± 0.07	14.3	2.19	-	4.07 ± 0.73
MACS J0647.7+7015	0.584	06 : 47 : 50.65	+70 : 14 : 53.99	F160W	1.44	56.9 ± 0.29	14.3	14.70	-	7.71 ± 2.77
MACS J0744.9+3927	0.686	07 : 44 : 52.80	+39 : 27 : 26.74	F160W	2.47	14.7 ± 0.09	14.3	7.74	-	7.65 ± 2.45

^a Cluster redshift and sky coordinates.

^b *HST* band corresponding to the rest-frame wavelength of $1\mu\text{m}$.

^c Sérsic index of the BCG obtained with GALFIT in the *HST* band corresponding to the rest-frame wavelength of $1\mu\text{m}$.

^d Effective radius of the BCG obtained with GALFIT in the *HST* band corresponding to the rest-frame wavelength of $1\mu\text{m}$.

^e BCG centric radius for M_{star} , M_{gas} , and M_{tot} estimates.

^f BCG total stellar mass $M_{\text{star}}(< r)$ estimated by [Cooke et al. \(2016\)](#). We assume a fractional uncertainty of 10% in our analysis.

^g X-ray gas mass $M_{\text{gas}}(< r)$ from [Donahue et al. \(2014\)](#).

^h Lensing mass $M_{\text{tot}}(< r)$ from [Umetsu et al. \(2016\)](#).

We define the hot gas fraction as $f_{\text{gas}}(r) = M_{\text{gas}}(< r)/M_{\text{tot}}(< r)$, the ratio of the gas mass $M_{\text{gas}}(< r)$ to the total mass $M_{\text{tot}}(< r)$ as a function of the cluster-centric radius r . For each cluster, we evaluate $M_{\text{tot}}(< r)$ and $f_{\text{gas}}(r)$ where the *Chandra* gas mass measurements $M_{\text{gas}}(< r)$ of [Donahue et al. \(2014\)](#) are available.

In the upper panel of Figure 1, we show the hot gas fractions $f_{\text{gas}}(r)$ of all individual clusters in our CLASH sample, along with the mean profile $\langle f_{\text{gas}}(r) \rangle$ of the sample. The mean $\langle f_{\text{gas}}(r) \rangle$ increases with increasing cluster-centric radius r , approaching the cosmic baryon fraction $\Omega_b/\Omega_m = (15.7 \pm 0.4)\%$ ([Planck Collaboration et al. 2016](#)) at $r \gtrsim 700$ kpc $\sim 0.5r_{500}$.

We note that [Donahue et al. \(2014\)](#) derived the hot gas fractions of CLASH clusters by combining their X-ray gas mass measurements with earlier CLASH weak-lensing results from [Umetsu et al. \(2014\)](#) or [Merten et al. \(2015\)](#). Our results improve upon those of [Donahue et al. \(2014\)](#) by using the full-lensing constraints of [Umetsu et al. \(2016\)](#) based on CLASH strong-lensing, weak-lensing shear and magnification data.

3.2. Baryon Fraction

We compute for each cluster the baryon fraction $f_{\text{bar}}(r) = M_{\text{bar}}(< r)/M_{\text{tot}}(< r)$ as a function of r . The baryonic cluster mass $M_{\text{bar}}(< r)$ consists of the X-ray gas mass $M_{\text{gas}}(< r)$ from [Donahue et al. \(2014\)](#), the stellar mass estimated as $M_{\text{star}}(< r) = M_{\text{gas}}(< r) \times f_c(r)/[1 - f_c(r)]$ (Section 2.2), and the stellar mass of the BCG in the innermost cluster region (Section 2.3). As in Section 3.1, we evaluate for each cluster $M_{\text{tot}}(< r)$ and $f_{\text{bar}}(r)$ where the *Chandra* $M_{\text{gas}}(< r)$ values of [Donahue et al. \(2014\)](#) are available.

For each cluster, we also include a single constraint on the baryon fraction $f_{\text{bar}}(< r)$ in the central BCG region. The stellar mass distribution of each BCG is modeled by Equation

(5), as described in Section 2.3. For 13 clusters in our sample, we have *Chandra* M_{gas} measurements ([Donahue et al. 2014](#)) lying in the central BCG region at $r < \langle R_e \rangle \sim 30$ kpc (see Table 1). For these clusters, we calculate the BCG stellar mass $m_{\text{star}}(< r)$ at this innermost radius of the *Chandra* M_{gas} measurements (Table 1). For the other clusters, we calculate $m_{\text{star}}(< r)$ at $r_{\text{min}} \simeq 14$ kpc and ignore the gas mass contribution to $M_{\text{bar}}(< r_{\text{min}})$. We note that, typically, the hot gas contribution in the innermost region $r < R_e$ is subdominant compared to the BCG stellar mass (e.g., [Sartoris et al. 2020](#)).

In the lower panel of Figure 1, we show the baryon fraction profiles $f_{\text{bar}}(r)$ outside the BCG region for all individual clusters in our sample. The mean $\langle f_{\text{bar}}(r) \rangle$ profile of the sample is nearly constant $\sim 1/8$ ([Donahue et al. 2014](#)) with r . The cluster-to-cluster scatter around the mean $f_{\text{bar}}(r)$ profile is 0.041 in terms of the standard deviation, and the total baryon fractions in some clusters reach the cosmic mean value. We do not find any clear radial trend in the baryon fraction profiles $f_{\text{bar}}(r)$ for the CLASH sample, as in the case of spiral galaxies ([McGaugh 2004; Famaey & McGaugh 2012](#)).

At $r = 800$ kpc $\sim 0.6r_{500}$ (the maximum radius of our ensemble measurements), the mean baryon fraction of the CLASH sample is $\langle f_{\text{bar}} \rangle = (14.2 \pm 1.4)\%$, which corresponds to a depletion factor of $\mathcal{D} \equiv 1 - f_{\text{bar}}/(\Omega_b/\Omega_m) = (10 \pm 9)\%$ with respect to the cosmic mean value, $\Omega_b/\Omega_m = (15.7 \pm 0.4)\%$. This level of depletion is not statistically significant, and it is in agreement with $\mathcal{D} = (18 \pm 2)\%$ at $r = r_{500}$ found from an independent constraint on the SPT sample by [Chiu et al. \(2018\)](#), as well as with the results from numerical simulations, $\mathcal{D} = 10\%-20\%$ (e.g., [McCarthy et al. 2011; Barnes et al. 2017](#)). Moreover, since the hot gas is more extended than DM, the gas fraction $f_{\text{gas}}(r)$ increases with cluster-centric radius r , so that the depletion factor of the CLASH sample at

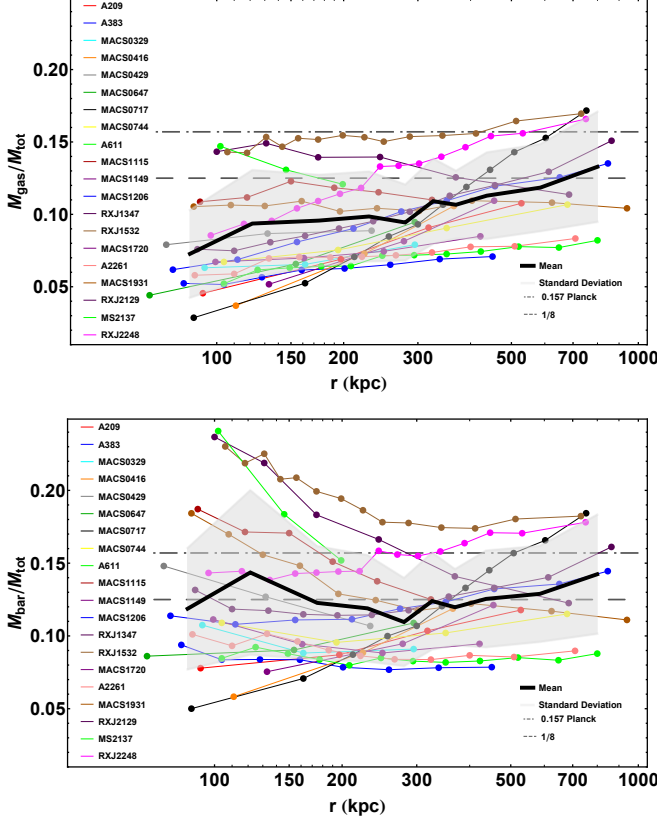


Figure 1. Upper panel: the hot gas fraction $f_{\text{gas}}(r) = M_{\text{gas}}(< r)/M_{\text{tot}}(< r)$ as a function of the cluster-centric radius r for 20 CLASH clusters in our sample. Lower panel: the total baryon fraction $f_{\text{bar}}(r) = M_{\text{bar}}(< r)/M_{\text{tot}}(< r)$ where M_{bar} includes the X-ray emitting hot gas mass M_{gas} and the stellar mass M_{star} . The 20 CLASH clusters are labeled with different colors. In each panel, the thick black solid line shows the mean profile of the sample, and the gray shaded area represents the standard deviation from the mean. The horizontal dot-dashed line shows the cosmic mean baryon fraction Ω_b/Ω_m (Planck Collaboration et al. 2016), and the horizontal dashed line corresponds to $1/8$.

r_{500} is expected to be much less significant.

3.3. Radial Acceleration Relation in CLASH Galaxy Clusters

Here we quantify and characterize the relationship between the total acceleration $g_{\text{tot}}(r)$ and the baryonic acceleration $g_{\text{bar}}(r)$ for the CLASH sample (Figure 1). To this end, for each cluster, we extract data points where possible at $r = 100$ kpc (18 clusters), 200 kpc (20 clusters), 400 kpc (15 clusters), and 600 kpc (11 clusters), by using linear interpolation. These data points are sufficiently well separated from each other. Hence, for simplicity, we ignore covariances between different radial bins in our fitting procedure. Altogether, we have a total of 84 data points for our sample of 20 CLASH clusters, including 20 data points in the central BCG region.

Since the mass ratio $M_{\text{tot}}(< r)/M_{\text{bar}}(< r)$ is equivalent to the acceleration ratio $g_{\text{tot}}(r)/g_{\text{bar}}(r)$, the MDAR can be expressed as a relation between $g_{\text{tot}}(r)/g_{\text{bar}}(r)$ and g_{bar} . In spiral galaxies, there exists a tight empirical relationship between the observed total acceleration $g_{\text{tot}}(r)$ and the baryonic acceleration $g_{\text{bar}}(r)$, namely the RAR (McGaugh et al. 2016). In fact, the MDAR and RAR are mathematically equivalent. However, we point out that in the RAR, values of each of the two axes come from independent measurements.

We present our results in the form of the RAR. We model

the CLASH data distribution in log-acceleration space by performing a linear regression on the relation $y = mx + b$ with $y = \ln(g_{\text{tot}}/g_0)$ and $x = \ln(g_{\text{bar}}/g_0)$ with a normalization scale of $g_0 = 1 \text{ m s}^{-2}$.⁵ Here we account for the uncertainties in the determinations of lensing mass $M_{\text{tot}}(< r)$, gas mass $M_{\text{gas}}(< r)$, and stellar mass $m_{\text{star}}(< r)$ of the BCG (see Section 2). The uncertainties in x and y are expressed as $\sigma_x = \sigma(M_{\text{tot}})/M_{\text{tot}}$ and $\sigma_y = \sigma(M_{\text{bar}})/M_{\text{bar}}$, where $\sigma(M_{\text{tot}})$ and $\sigma(M_{\text{bar}})$ are the total uncertainties for the lensing and baryonic mass estimates M_{tot} and M_{bar} , respectively.

The log-likelihood function is written as

$$-2 \ln \mathcal{L} = \sum_i \ln(2\pi\sigma_i^2) + \sum_i \frac{[y_i - (mx_i + b)]^2}{\sigma_i^2}, \quad (6)$$

where i runs over all clusters and data points, and σ_i includes the observational uncertainties ($\sigma_{x_i}, \sigma_{y_i}$) and lognormal intrinsic scatter σ_{int} (e.g., see Umetsu et al. 2016; Okabe & Smith 2016),

$$\sigma_i^2 = \sigma_{y_i}^2 + m^2 \sigma_{x_i}^2 + \sigma_{\text{int}}^2. \quad (7)$$

The σ_{int} parameter accounts for the intrinsic scatter around the mean RAR due to unaccounted astrophysics associated with the RAR.

We perform a Markov chain Monte Carlo (MCMC) analysis to constrain the regression parameters using the emcee python package (Foreman-Mackey et al. 2013, 2019) based on an affine-invariant sampler (Goodman & Weare 2010). We use non-informative uniform priors on b and m of $b \in [-100, 100]$ and $m \in [-100, 100]$. For the intrinsic scatter, we assume a prior that is uniform in $\ln \sigma_{\text{int}}$ in the range $\ln \sigma_{\text{int}} \in [-5, 1]$. Using the MCMC technique, we sample the posterior probability distributions of the regression parameters ($b, m, \sigma_{\text{int}}$) over the full parameter space allowed by the priors.

From the regression analysis, we find a tight RAR for the CLASH sample in the BCG-cluster regime. Figure 2 summarizes our results. In the left panel, we show the distribution of CLASH clusters in $\log_{10} g_{\text{bar}} - \log_{10} g_{\text{tot}}$ space along with the best-fit relation (black solid line). The spread of the best-fit residuals is about 0.11 dex, as shown in the inset plot of Figure 2. The resulting constraints on the regression parameters are $m = 0.51^{+0.04}_{-0.05}$, $b = -9.80^{+1.07}_{-1.08}$, and $\sigma_{\text{int}} = 14.7^{+2.9\%}_{-2.8\%}$ in terms of the MCMC-sampled posterior mean and standard deviation. The RAR for the CLASH sample is summarized as

$$\ln(g_{\text{tot}}/\text{m s}^{-2}) = 0.51^{+0.04}_{-0.05} \ln(g_{\text{bar}}/\text{m s}^{-2}) - 9.80^{+1.07}_{-1.08}. \quad (8)$$

Figure 2 also compares our results with the RAR in spiral galaxies from McGaugh et al. (2016, dashed line). The slope we obtained $m = 0.51^{+0.04}_{-0.05}$ is consistent with the low acceleration limit $1/2$ of the RAR from McGaugh et al. (2016), $g_{\text{tot}} = \sqrt{g_{\ddagger} g_{\text{bar}}}$ with $g_{\ddagger} \simeq 1.2 \times 10^{-10} \text{ m s}^{-2}$. On the other hand, the intercept b at fixed g_{bar} is found to be significantly higher than that of McGaugh et al. (2016).

Here we repeat our regression analysis by fixing the slope to $m = 1/2$ and rewriting the scaling relation as $g_{\text{tot}}(r) = \sqrt{g_{\ddagger} g_{\text{bar}}(r)}$ with g_{\ddagger} a constant acceleration that corresponds

⁵ We note that the resulting RAR is presented in decimal logarithmic units (\log_{10}) in Figures 1 and 3, whereas our regression analysis uses the natural logarithm (\ln) of acceleration.

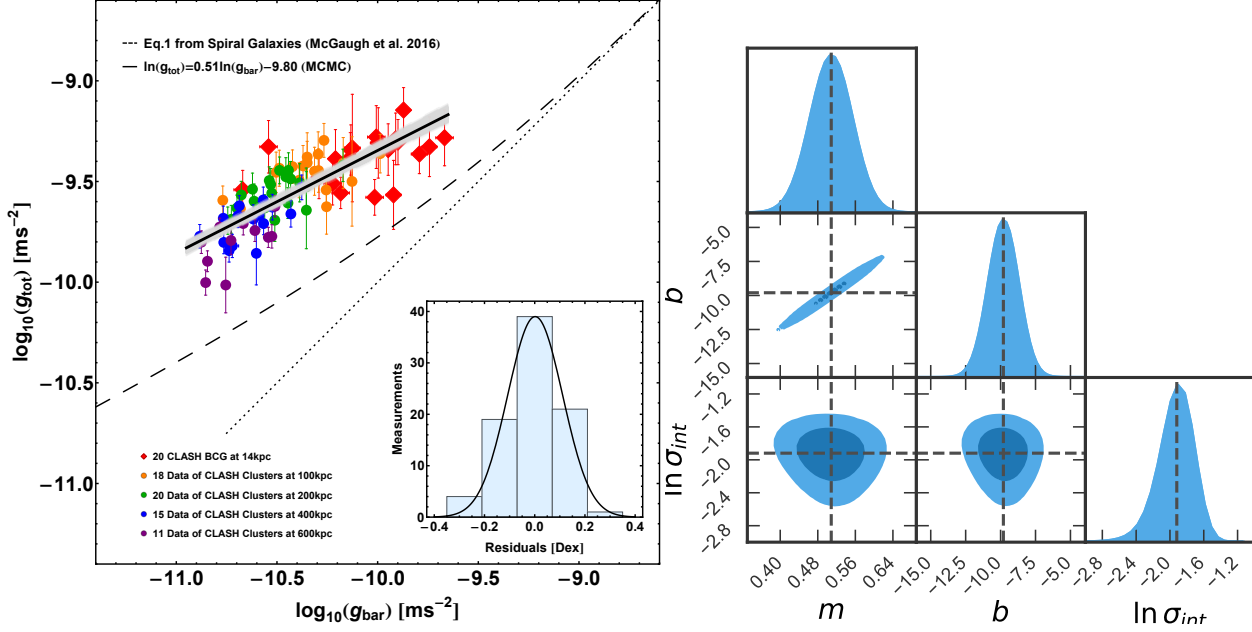


Figure 2. Radial acceleration relation (RAR) in 20 CLASH galaxy clusters from the central BCG to the intra-cluster regime. Left panel: a comparison of the total acceleration $g_{\text{tot}}(r) = GM_{\text{tot}}(<r)/r^2$ from gravitational lensing and the baryonic acceleration $g_{\text{bar}}(r) = GM_{\text{bar}}(<r)/r^2$ which includes the hot-gas and stellar mass contributions to the baryonic mass $M_{\text{bar}}(<r)$. The red diamonds with error bars represent the measurements in the central BCGs for all 20 CLASH clusters in our sample. The orange, green, blue, and purple circles with error bars show the measurements in the intra-cluster regime at $r = 100, 200, 400$, and 600 kpc, respectively. The gray shaded area represents the 1σ range around the best-fitting relation shown with the black solid line. The black dashed line shows Equation (1) of McGaugh et al. (2016). The black dotted line shows the one-to-one relation, $g_{\text{tot}} = g_{\text{bar}}$. The inset plot shows the histogram distribution of best-fit residuals, which is characterized by a 0.11 dex scatter. Right panel: constraints on the regression parameters for the RAR in the CLASH sample, showing marginalized one-dimensional (histograms) and two-dimensional posterior distributions.

to a certain characteristic acceleration scale. Then, the regression parameters are constrained as $g_{\ddagger} = (2.02 \pm 0.11) \times 10^{-9} \text{ m s}^{-2}$, and $\sigma_{\text{int}} = 14.5^{+2.9}_{-2.8}\%$.

4. DISCUSSION

4.1. Interpretation of the CLASH RAR in the Λ CDM framework

Using a semi-analytical model with abundance matching, Navarro et al. (2017) provided a possible explanation of the RAR in spiral galaxies within the Λ CDM framework. Here we test if the observed RAR for the CLASH sample can be explained by a semi-analytical description of cluster-scale halos in the standard Λ CDM model. Unlike the RAR in spiral galaxies based on stellar kinematics, the total acceleration g_{tot} in the CLASH sample has been derived assuming the NFW density profile. Our data points and semi-analytical model are thus not entirely independent in terms of the profile shape of DM.

To this end, we employ the semi-analytical model of Olamaie et al. (2012), which describes the distributions of DM and hot gas with an ideal gas equation of state in a spherical cluster halo. First, this model assumes that DM follows the NFW profile (Umetsu et al. 2011a, 2016; Niikura et al. 2015; Okabe & Smith 2016) and the gas pressure is described by a generalized NFW profile (Nagai et al. 2007). Following Olamaie et al. (2012), we fix the values of the gas concentration and slope parameters of the generalized NFW profile to those found by Arnaud et al. (2010). Next, the system is assumed to be in hydrostatic equilibrium. We then assume a gas mass fraction of $f_{\text{gas}}(r_{500}) = 13\%$ (e.g., Planck Collaboration et al. 2013; Donahue et al. 2014) at $r = r_{500}$ to fix the normalization of $\rho_{\text{gas}}(r)$. Finally, in these calculations,

we assume that the gas density ρ_{gas} is much smaller than the DM density ρ_{DM} , $\rho_{\text{tot}}(r) = \rho_{\text{DM}}(r) + \rho_{\text{gas}}(r) \approx \rho_{\text{DM}}(r)$. With these assumptions, $\rho_{\text{gas}}(r)$ can be fully specified by two parameters that describe the NFW density profile. We refer to Olamaie et al. (2012) for full details of the model.

Following the procedure outlined above, we can describe the average properties of our cluster sample, which includes 16 X-ray-selected and 4 high-magnification-selected CLASH clusters of Umetsu et al. (2016). Here we adopt $M_{200} = 1.55 \times 10^{15} M_{\odot}$ and $c_{200} = 3.28$ to describe the DM distribution $\rho_{\text{DM}}(r)$ of our sample with a median redshift of $z = 0.377$. Given the NFW parameters, we compute the gas density profile $\rho_{\text{gas}}(r)$ for the CLASH sample. We use $f_c(r)$ of Chiu et al. (2018) (Section 2.2) to account for the stellar mass contribution to the baryonic mass. With these average profiles $\rho_{\text{DM}}(r)$, $\rho_{\text{gas}}(r)$, and f_c , we can predict the total and baryonic gravitational acceleration profiles, $g_{\text{tot}}(r)$ and $g_{\text{bar}}(r)$, for the CLASH sample. Here we compute the acceleration profiles at $r = 100, 200, 400$, and 600 kpc, as done in our CLASH analysis.

We also model the intrinsic scatter around the average profiles $g_{\text{tot}}(r)$ and $g_{\text{bar}}(r)$ due to cluster-to-cluster variations in the DM and baryonic distributions. For the DM distribution, we assign intrinsic scatter in c_{200} with a lognormal intrinsic dispersion of 30% (e.g., Bhattacharya et al. 2013). For the baryonic distribution, we assign intrinsic scatter in f_c with a Gaussian dispersion of 12% (Chiu et al. 2018). We employ Monte-Carlo simulations to evaluate the intrinsic dispersions around the average acceleration profiles $g_{\text{tot}}(r)$ and $g_{\text{bar}}(r)$ at each cluster-centric radius. The result is shown in Figure 3.

The 20 galaxy clusters in our sample are all high-mass systems selected for the CLASH survey (Postman et al. 2012). It is thus reasonable to adopt a set of average properties in the

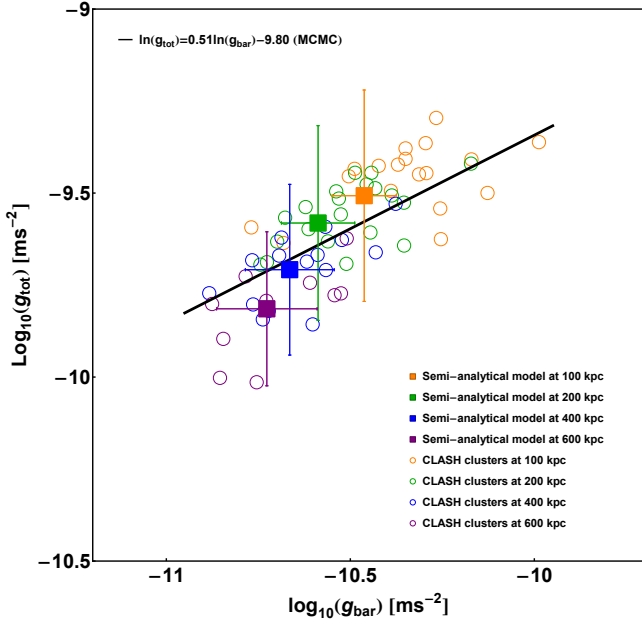


Figure 3. Predictions for the CLASH radial acceleration relation (RAR) from semi-analytic modeling in the Λ CDM framework. The orange, green, blue, and purple squares show the model predictions for the CLASH sample at $r = 100, 200, 400$, and 600 kpc, respectively, and the error bars represent the 1σ intrinsic scatter. Open circles show the measurements for the CLASH sample (Figure 2).

semi-analytical model to study the new RAR. As shown in Figure 3, all the model points (color-coded squares) match the distribution of data points (color open circles) and the mean relation (black solid line) well.

The inferred level of 1σ intrinsic scatter estimated by Monte-Carlo simulations appears to be larger than the data distribution. This is similar to the findings in spiral galaxies (see, e.g., Di Cintio & Lelli 2016; Desmond 2017; Lelli et al. 2017). However, it should be noted that the CLASH sample is dominated by relaxed systems (Meneghetti et al. 2014) because of the CLASH selection based on X-ray morphology regularity (Postman et al. 2012). As a result, the CLASH sample is predicted to have a much smaller level of intrinsic scatter in the $c_{200}-M_{200}$ relation (16%; Meneghetti et al. 2014; Umetsu et al. 2016).

The CLASH RAR (Equation (8)) expresses $g_{\text{tot}}(r)$ as a function of $g_{\text{bar}}(r)$. Thus, one can obtain the baryon fraction $f_{\text{bar}}(r)$ if $g_{\text{bar}}(r)$ is known, because $f_{\text{bar}}(r) = M_{\text{bar}}(< r)/M_{\text{tot}}(< r) = g_{\text{bar}}(r)/g_{\text{tot}}(r)$. If we approximate the CLASH RAR as $g_{\text{tot}} \approx \sqrt{g_{\text{bar}}}$, then the baryon fraction has the simple form,

$$f_{\text{bar}}(r) \approx \sqrt{g_{\text{bar}}(r)/g_{\text{tot}}}. \quad (9)$$

Since the 20 CLASH clusters in our sample are of similar size and acceleration profile, we can infer an average relation between the baryonic acceleration g_{bar} and the cluster-centric radius r . Making use of the X-ray gas mass measurements from Donahue et al. (2014) and the stellar mass correction from Chiu et al. (2018), we obtain such an average relation, i.e., the average baryonic acceleration as a function of r , $\langle g_{\text{bar}}(r) \rangle$. Then, the best-fit CLASH RAR (Equation (8)) together with $\langle g_{\text{bar}}(r) \rangle$ gives an empirical relation for the baryon fraction as a function of r .

In Figure 4, we compare the $f_{\text{bar}}(r)$ profile inferred from the best-fit CLASH RAR (Equation (8)) with the observed

distribution of CLASH baryon fractions shown in Figure 1. The gray circles are the inferred baryon fractions at different cluster-centric radii, r . The thick black line shows the observed mean $\langle f_{\text{bar}}(r) \rangle$ profile averaged over the CLASH sample (see Figure 1). The $f_{\text{bar}}(r)$ profile inferred from the best-fit RAR and the mean $\langle f_{\text{bar}}(r) \rangle$ profile for the CLASH sample are consistent within $r = 400$ kpc, but deviate from each other beyond 400 kpc. This is because the best-fit RAR model predicts a radially decreasing $f_{\text{bar}}(r)$ profile, whereas the observed CLASH $\langle f_{\text{bar}}(r) \rangle$ profile is nearly constant ($\sim 1/8$; see Figure 1) in the intracluster regime.

We also compare these baryon fraction profiles with the corresponding values predicted by our semi-analytical model, which are denoted by the orange, green, blue and purple squares for $r = 100, 200, 400$, and 600 kpc, respectively. The values of all model points agree well with the best-fit RAR and the observed mean values for the CLASH sample. Our semi-analytical model predicts a nearly constant $f_{\text{bar}}(r)$ profile, in good agreement with the mean relation of the CLASH sample (black solid line).

To assess how the data deviate from the best-fit CLASH RAR, we show in Figure 5 the distribution of best-fit residuals as a function of cluster radius r . We note again that both the semi-analytical model and the CLASH RAR assume the NFW density profile for the total matter distribution. The residuals are defined as the difference of $\log_{10}(g_{\text{tot}})$ between the observational data and the best-fit RAR (Equation (8)). As shown in the figure, the residuals at small r ($\approx 14, 100$, and 200 kpc) distribute symmetrically across the best-fit RAR (the zero residual line). However, at larger cluster radii $r \gtrsim 400$ kpc, the residuals deviate systematically toward negative values. The semi-analytical model (color-coded squares) exhibits a similar trend as seen for the observational data.

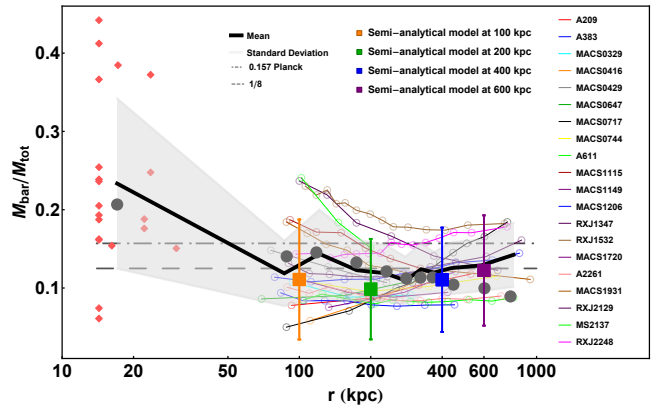


Figure 4. Comparison of the observed and predicted total baryon fraction profiles $f_{\text{bar}}(r) = M_{\text{bar}}(< r)/M_{\text{tot}}(< r)$ for the CLASH sample. The red diamonds and color-coded lines represent the CLASH observational constraints in the BCG and cluster regions, respectively. The gray circles show empirical predictions based on the best-fit CLASH RAR (see Equation (8)) combined with the mean value of baryonic acceleration $\langle g_{\text{bar}}(r) \rangle$ at each cluster radius. The thick black line shows the mean $\langle f_{\text{bar}}(r) \rangle$ profile averaged over the CLASH sample. The orange, green, blue, and purple squares represent predictions from a semi-analytical model at 100, 200, 400, and 600 kpc respectively, and the error bars show the 1σ intrinsic scatter.

4.2. Implications for Residual Missing Mass in MOND

As discussed earlier, Equation (1) in the MOND framework is consistent with the observed RAR on galaxy scales with $g_{\text{bar}} \equiv g_{\text{M}}$, without introducing DM. Here we test this hypothesis with our CLASH RAR results and infer the level of

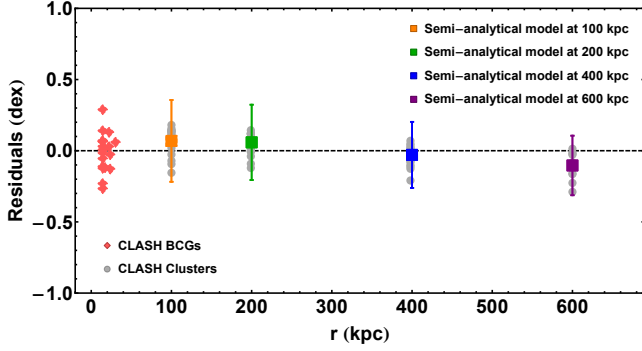


Figure 5. Residuals of the best-fit RAR for the CLASH sample as a function of the cluster-centric radius r . The vertical axis represents the difference between the data and the best-fit RAR in units of dex. The horizontal axis is the cluster-centric radius r in units of kpc. The red diamonds and the gray filled circles denote the CLASH measurements in the central BCG region and the intracluster region (100, 200, 400, and 600 kpc), respectively (see Figure 2). The orange, green, blue, and purple squares show the deviations of our semi-analytical predictions relative to the best-fit CLASH RAR, and the error bars show the 1σ intrinsic scatter.

residual missing mass on the BCG-cluster scale within the MOND framework.

Since the total acceleration g_{tot} in the CLASH RAR implies $g_{\text{tot}} \approx \sqrt{g_{\text{bar}} g_{\ddagger}}$, we can relate g_{bar} and g_{M} by

$$\sqrt{g_{\text{bar}} g_{\ddagger}} \approx \frac{g_{\text{M}}}{1 - e^{-\sqrt{g_{\text{M}}/g_{\ddagger}}}}. \quad (10)$$

The mass ratio between M_{M} and M_{bar} is $M_{\text{M}}/M_{\text{bar}} = g_{\text{M}}/g_{\text{bar}}$. Our formulation implies that the level of residual missing mass in MOND depends on the baryonic acceleration g_{bar} . In our CLASH data, the largest baryonic acceleration in the BCG regime is $2.1 \times 10^{-10} \text{ m s}^{-2}$ and the smallest one in the intracluster regime is $1.3 \times 10^{-11} \text{ m s}^{-2}$. The corresponding mass ratio $M_{\text{M}}/M_{\text{bar}}$ thus ranges from 2.7 to 7.3, increasing with decreasing baryonic acceleration g_{bar} (or increasing cluster-centric radius).

Hence, the CLASH RAR confirms the existence of residual missing mass in MOND on the BCG-cluster scale, as found in the literature (Sanders 1999, 2003; Pointecouteau & Silk 2005; Famaey & McGaugh 2012). Furthermore, it reveals a more substantial level of discrepancy or residual missing mass $M_{\text{M}}/M_{\text{bar}}$ in the low g_{bar} regime, which corresponding to the cluster outskirts. The typical level of residual missing mass found in the literature is $\langle M_{\text{M}}/M_{\text{bar}} \rangle \sim 2$. However, it should be note that a fair comparison of the CLASH RAR with MOND will require a relativistic extension of MOND to properly interpret the gravitational lensing data for the CLASH sample. Some possibilities in this approach for cluster lensing have been discussed in the literature (Bruneton et al. 2009; Zhao & Famaey 2012; Famaey & McGaugh 2012).

4.3. Implications for Kinematic Scaling Relations

We recall that the RAR in galaxies has a characteristic acceleration scale of $g_{\ddagger} \simeq 1.2 \times 10^{-10} \text{ m s}^{-2}$, above which the acceleration of the system asymptotically tends to Newtonian dynamics without DM (i.e., $g_{\text{tot}} = g_{\text{bar}}$), while below which the acceleration asymptotically tends to $g_{\text{tot}} = \sqrt{g_{\ddagger} g_{\text{bar}}}$. Our CLASH results indicate that $g_{\text{tot}} \approx \sqrt{g_{\ddagger} g_{\text{bar}}}$ (see Equation (9)) on BCG-cluster scales, with a characteristic acceleration scale of $g_{\ddagger} \gg g_{\ddagger}$. However, in our CLASH sample, it is not clear whether or not the acceleration of the system will approach to $g_{\text{tot}} = g_{\text{bar}}$ in the high acceleration limit, $g_{\text{bar}} \gg g_{\ddagger}$.

If the CLASH RAR holds in general for other galaxy clusters, then there exists a kinematic relation or law in galaxy clusters, in analogy to Kepler’s law of planetary motion that comes from Newtonian dynamics. Let us take the example of the baryonic Tully–Fisher relation (BTFR; e.g., McGaugh 2011, 2012; Famaey & McGaugh 2012), which comes from the low acceleration end of the RAR of spiral galaxies. In rotationally support systems such as spiral galaxies, the centripetal acceleration is provided by the total gravitational acceleration, i.e., $v^2/r = g_{\text{tot}}$ where v is the circular speed. In the small acceleration regime of $g_{\text{bar}} \ll g_{\ddagger}$, the RAR in galaxies gives $g_{\text{tot}} \approx \sqrt{g_{\ddagger} g_{\text{bar}}}$. By expressing the baryonic acceleration as $g_{\text{bar}} = GM_{\text{bar}}/r^2$ where M_{bar} is the total baryonic mass inside r , we obtain the BTFR, $v^4 = Gg_{\ddagger}M_{\text{bar}}$. For systems supported by random motions, such as elliptical galaxies and galaxy clusters, $g_{\text{tot}} \propto \sigma^2/r$ with σ_v the velocity dispersion. If a system that follows the RAR is in the low acceleration regime, $\sigma_v^4 \propto g_{\ddagger}M_{\text{bar}}$ is anticipated. We refer to this kinematic law as the baryonic Faber–Jackson relation (BFJR).

In the literature, the BFJR has not been confirmed in galaxy clusters. However, scaling relations between total cluster mass and X-ray mass proxies (e.g., X-ray gas temperature; Sanders 1994; Ettori et al. 2004; Angus et al. 2008; Famaey & McGaugh 2012), and that between X-ray luminosity and galaxy velocity dispersion (Xue & Wu 2000; Sanders 2010; Zhang et al. 2011; Nastasi et al. 2014), have been firmly established based on multiwavelength observations and numerical simulations. If the total baryonic mass in galaxy clusters is tightly coupled with thermodynamic properties of the hot gas in hydrostatic equilibrium, we may expect a correlation between the total baryonic mass and galaxy velocity dispersion.

5. SUMMARY

The radial acceleration relation (RAR) in galaxies represents a tight empirical scaling law between the total acceleration $g_{\text{tot}}(r) = GM_{\text{tot}}(< r)/r^2$ observed in galaxies and that expected from their baryonic mass $g_{\text{bar}}(r) = GM_{\text{bar}}(< r)/r^2$, with a characteristic acceleration scale of $g_{\ddagger} \simeq 1.2 \times 10^{-10} \text{ m s}^{-2}$ (McGaugh et al. 2016). The RAR observed on galaxy scales raised four fundamental issues to be explained (see Section 1; Desmond 2017; Lelli et al. 2017).

In this paper, we have examined if such a correlation exists in galaxy clusters using weak-lensing, strong-lensing, and X-ray data sets (Donahue et al. 2014; Umetsu et al. 2016) available for 20 high-mass clusters targeted by the CLASH survey (Postman et al. 2012). By combining our CLASH data sets with central baryonic mass in the BCG region and accounting for the stellar baryonic component in the intracluster region, we have discovered, for the first time, a tight RAR on BCG-cluster scales. The resulting RAR for the CLASH sample is well described by a power-law relation, $g_{\text{tot}} \propto g_{\text{bar}}^{0.51^{+0.04}_{-0.05}}$, with lognormal intrinsic scatter of $14.7^{+2.9}_{-2.8}\%$. The slope of the best-fit relation is consistent with the low acceleration limit of the RAR in galaxies, $g_{\text{tot}} = \sqrt{g_{\ddagger} g_{\text{bar}}}$, whereas the intercept implies a much higher acceleration scale of $g_{\ddagger} = (2.02 \pm 0.11) \times 10^{-9} \text{ m s}^{-2}$. Our results indicate that there is no universal RAR that holds on all scales from galaxies to clusters.

Regarding the issues raised by the RAR in galaxies, the CLASH RAR has: (1) an acceleration scale g_{\ddagger} that is much

higher than that in galaxies, $g_{\ddagger} \gg g_{\dagger}$; (2) the slope in the best-fit RAR is $0.51^{+0.04}_{-0.05}$, which matches the low acceleration limit of the RAR in galaxies (see Equation (2)); (3) the level of intrinsic scatter, $14.7^{+2.9}_{-2.8}\%$, is as tight as that in the RAR for galaxies. The best-fit residuals of the CLASH RAR exhibit a systematic radial trend at $r > 400$ kpc (Figure 5). The best-fit RAR model predicts a radially decreasing $f_{\text{bar}}(r)$ profile, whereas the CLASH data distribution is nearly constant (Figure 1) in the intracluster regime. To fully investigate the discrepancy at $g_{\text{bar}} \lesssim \times 10^{-11} \text{ m s}^{-2}$, or at $r \gtrsim 400$ kpc, we need additional data covering a broader range of acceleration on BCG-cluster scales.

We find that the observed RAR in CLASH clusters is consistent with predictions from semi-analytical modeling of cluster halos in the standard Λ CDM framework. Our results also predict the presence of a baryonic Faber–Jackson relation ($\sigma_v^4 \propto M_{\text{bar}}$) on cluster scales.

We are very grateful to Stacy McGaugh for stimulating discussions on this work. We thank Po-Chieh Yu for his help with the GALFIT analysis. We thank the anonymous referee for their valuable comments to improve the clarity of this paper. Y.T. and C.M.K. are supported by the Taiwan Ministry of Science and Technology grant MOST 105-2112-M-008-011-MY3 and MOST 108-2112-M-008-006. K.U. acknowledges support from the Ministry of Science and Technology of Taiwan (grant MOST 106-2628-M-001-003-MY3) and from the Academia Sinica Investigator Award (AS-IA-107-M01). We acknowledge the use of the pyGTC package (Bocquet & Carter 2016) for creating the right panel of Figure 2.

Note added in proof. We noted that while this paper was under review for publication, a paper by Chan & Del Popolo (2020) appeared on the arXiv preprint service. They analyzed X-ray data for a sample of X-ray-selected non-cool-core clusters and derived an RAR for their sample assuming hydrostatic equilibrium, without accounting for the stellar baryonic contribution. Although their results are not in quantitative agreement with ours, they also conclude that the RAR is unlikely to be universal and scale independent.

REFERENCES

- Angus, G. W., Famaey, B., & Buote, D. A. 2008, *MNRAS*, **387**, 1470
- Arnaud, M., Pratt, G. W., Piffaretti, R., et al. 2010, *A&A*, **517**, A92
- Barnes, D. J., Kay, S. T., Bahé, Y. M., et al. 2017, *MNRAS*, **471**, 1088
- Behroozi, P. S., Wechsler, R. H., & Conroy, C. 2013, *ApJ*, **770**, 57
- Bhattacharya, S., Habib, S., Heitmann, K., & Vikhlinin, A. 2013, *ApJ*, **766**, 32
- Blanchet, L., & Le Tiec, A. 2008, *Phys. Rev. D*, **78**, 024031
- . 2009, *Phys. Rev. D*, **80**, 023524
- Blemer, L. E., Stalder, B., de Haan, T., et al. 2015, *ApJS*, **216**, 27
- Bocquet, S., & Carter, F. W. 2016, *The Journal of Open Source Software*, **1**
- Bruneton, J.-P., Liberati, S., Sindoni, L., & Famaey, B. 2009, *J. Cosmology Astropart. Phys.*, **2009**, 021
- Carlstrom, J. E., Ade, P. A. R., Aird, K. A., et al. 2011, *PASP*, **123**, 568
- Chae, K.-H., Bernardi, M., Sheth, R. K., & Gong, I.-T. 2019, *ApJ*, **877**, 18
- Chan, M. H., & Del Popolo, A. 2020, *MNRAS*, **492**, 5865
- Chiu, I. N., Umetsu, K., Sereno, M., et al. 2018, *ApJ*, **860**, 126
- Cooke, K. C., O’Dea, C. P., Baum, S. A., et al. 2016, *ApJ*, **833**, 224
- Desmond, H. 2017, *MNRAS*, **464**, 4160
- Di Cintio, A., & Lelli, F. 2016, *MNRAS*, **456**, L127
- Donahue, M., Voit, G. M., Mahdavi, A., et al. 2014, *ApJ*, **794**, 136
- Donahue, M., Connor, T., Fogarty, K., et al. 2015, *ApJ*, **805**, 174
- Ettori, S., Tozzi, P., Borgani, S., & Rosati, P. 2004, *A&A*, **417**, 13
- Famaey, B., & McGaugh, S. S. 2012, *Living Reviews in Relativity*, **15**, 10
- Farahi, A., Guglielmo, V., Evrard, A. E., et al. 2018, *A&A*, **620**, A8
- Foreman-Mackey, D., Hogg, D. W., Lang, D., & Goodman, J. 2013, *PASP*, **125**, 306
- Foreman-Mackey, D., Farr, W., Sinha, M., et al. 2019, *The Journal of Open Source Software*, **4**, 1864
- Goodman, J., & Weare, J. 2010, *Communications in Applied Mathematics and Computational Science*, **5**, 65
- Hernquist, L. 1990, *ApJ*, **356**, 359
- Hjorth, J., & Williams, L. L. R. 2010, *ApJ*, **722**, 851
- Janz, J., Cappellari, M., Romanowsky, A. J., et al. 2016, *MNRAS*, **461**, 2367
- Khouri, J. 2015, *Phys. Rev. D*, **91**, 024022
- Lelli, F., McGaugh, S. S., & Schombert, J. M. 2016, *AJ*, **152**, 157
- Lelli, F., McGaugh, S. S., Schombert, J. M., & Pawłowski, M. S. 2017, *ApJ*, **836**, 152
- Li, P., Lelli, F., McGaugh, S., & Schombert, J. 2018, *A&A*, **615**, A3
- Ludlow, A. D., Benítez-Llambay, A., Schaller, M., et al. 2017, *Phys. Rev. Lett.*, **118**, 161103
- McCarthy, I. G., Schaye, J., Bower, R. G., et al. 2011, *MNRAS*, **412**, 1965
- McGaugh, S. S. 2004, *ApJ*, **609**, 652
- . 2011, *Phys. Rev. Lett.*, **106**, 121303
- . 2012, *AJ*, **143**, 40
- McGaugh, S. S., Lelli, F., & Schombert, J. M. 2016, *Phys. Rev. Lett.*, **117**, 201101
- Meneghetti, M., Rasia, E., Vega, J., et al. 2014, *ApJ*, **797**, 34
- Merten, J., Meneghetti, M., Postman, M., et al. 2015, *ApJ*, **806**, 4
- Milgrom, M. 1983, *ApJ*, **270**, 365
- . 2019, *Phys. Rev. D*, **99**, 044041
- Miyatake, H., Battaglia, N., Hilton, M., et al. 2019, *ApJ*, **875**, 63
- Nagai, D., Kravtsov, A. V., & Vikhlinin, A. 2007, *ApJ*, **668**, 1
- Nastasi, A., Böhringer, H., Fassbender, R., et al. 2014, *A&A*, **564**, A17
- Navarro, J. F., Benítez-Llambay, A., Fattahi, A., et al. 2017, *MNRAS*, **471**, 1841
- Navarro, J. F., Frenk, C. S., & White, S. D. M. 1997, *ApJ*, **490**, 493
- Newman, A. B., Treu, T., Ellis, R. S., et al. 2013, *ApJ*, **765**, 24
- Niikura, H., Takada, M., Okabe, N., Martino, R., & Takahashi, R. 2015, *PASJ*, **67**, 103
- Okabe, N., & Smith, G. P. 2016, *MNRAS*, **461**, 3794
- Okabe, N., Umetsu, K., Tamura, T., et al. 2014, *PASJ*, **66**, 99
- Olamaie, M., Hobson, M. P., & Grainge, K. J. B. 2012, *MNRAS*, **423**, 1534
- Peng, C. Y., Ho, L. C., Impey, C. D., & Rix, H.-W. 2010, *AJ*, **139**, 2097
- Planck Collaboration, Ade, P. A. R., Aghanim, N., et al. 2013, *A&A*, **550**, A131
- . 2016, *A&A*, **594**, A13
- Pointecouteau, E., & Silk, J. 2005, *MNRAS*, **364**, 654
- Postman, M., Coc, D., Benítez, N., et al. 2012, *ApJS*, **199**, 25
- Rong, Y., Li, H., Wang, J., et al. 2018, *MNRAS*, **477**, 230
- Sanders, R. H. 1994, *A&A*, **284**, L31
- . 1999, *ApJL*, **512**, L23
- . 2003, *MNRAS*, **342**, 901
- . 2010, *MNRAS*, **407**, 1128
- Sartoris, B., Biviano, A., Rosati, P., et al. 2020, arXiv e-prints, arXiv:2003.08475
- Scarpa, R. 2006, in *American Institute of Physics Conference Series*, Vol. **822**, *First Crisis in Cosmology Conference*, ed. E. J. Lerner & J. B. Almeida, 253
- Sereno, M., Umetsu, K., Ettori, S., et al. 2018, *ApJL*, **860**, L4
- Shull, J. M., Smith, B. D., & Danforth, C. W. 2012, *ApJ*, **759**, 23
- Tian, Y., & Ko, C.-M. 2016, *MNRAS*, **462**, 1092
- . 2017, *MNRAS*, **472**, 765
- . 2019, *MNRAS*, **488**, L41
- Umetsu, K., Broadhurst, T., Zitrin, A., et al. 2011a, *ApJ*, **738**, 41
- Umetsu, K., Broadhurst, T., Zitrin, A., Medezinski, E., & Hsu, L.-Y. 2011b, *ApJ*, **729**, 127
- Umetsu, K., & Diemer, B. 2017, *ApJ*, **836**, 231
- Umetsu, K., Zitrin, A., Gruen, D., et al. 2016, *ApJ*, **821**, 116
- Umetsu, K., Birkinshaw, M., Liu, G.-C., et al. 2009, *ApJ*, **694**, 1643
- Umetsu, K., Medezinski, E., Nonino, M., et al. 2014, *ApJ*, **795**, 163
- Umetsu, K., Sereno, M., Lieu, M., et al. 2020, *ApJ*, **890**, 148
- Vikhlinin, A., Kravtsov, A., Forman, W., et al. 2006, *ApJ*, **640**, 691
- Wilson, S., Hilton, M., Rooney, P. J., et al. 2016, *MNRAS*, **463**, 413
- Wu, X., & Kroupa, P. 2015, *MNRAS*, **446**, 330
- Wu, X.-P., Fang, L.-Z., & Xu, W. 1998, *A&A*, **338**, 813
- Xue, Y.-J., & Wu, X.-P. 2000, *ApJ*, **538**, 65
- Zhang, Y. Y., Andernach, H., Caretta, C. A., et al. 2011, *A&A*, **526**, A105
- Zhao, H., & Famaey, B. 2012, *Phys. Rev. D*, **86**, 067301
- Zhao, H., & Li, B. 2010, *ApJ*, **712**, 130
- Zitrin, A., Fabris, A., Merten, J., et al. 2015, *ApJ*, **801**, 44
- Zwicky, F. 1933, *Helvetica Physica Acta*, **6**, 110